machines

MDPI

*Article*

# Establishing the Importance of Operating Temperature in the Structural Integrity of Large-Scale Direct-Drive Wind Turbine Generators

**Magnus Bichan *, Andrew Jack and Pablo Jaen-Sola ***

School of Computing, Engineering and the Built Environment, Edinburgh Napier University, 10 Colinton Road, Edinburgh EH10 5DT, UK

* Correspondence: magnus.bichan@napier.ac.uk (M.B.); p.sola@napier.ac.uk (P.J.-S.)

**Abstract:** Direct-drive generators are recognised for their low maintenance compared with conventional drivetrains, largely due to their fewer working parts. However, consequent to low-speed operation, these machines necessitate large diameters and are subject to rigorous stiffness requirements. Significant internal and external forces influence structural integrity, so to design them efficiently, consideration of all operating parameters is imperative. Therefore, through Finite Element Analysis, this paper sets out to quantify the influence of each operating parameter on the integrity of a parametrically optimised rotor structure under established operating conditions and introduces operating temperature to the current models. An environmental impact analysis of the optimised rotor structure and cost analyses of both the optimised and unaltered structures are carried out simultaneous to the design process. We find the use of parameter optimisation alone to be insufficient for rotor structures of this scale due to high increased mass and costs of manufacture. A significant finding from this study is that the thermal effects on large-scale direct-drive generator structures may be vastly underestimated and have a much greater influence on structural integrity than first thought.

**Keywords:** rotor structure; parametric optimisation; thermal analysis; life-cycle analysis; cost analysis



**Citation:** Bichan, M.; Jack, A.; Jaen-Sola, P. Establishing the Importance of Operating Temperature in the Structural Integrity of Large-Scale Direct-Drive Wind Turbine Generators. *Machines* **2023**, *11*, 780. https://doi.org/10.3390/machines11080780

Academic Editors: Francesco Castellani and Davide Astolfi

Received: 5 June 2023
Revised: 19 July 2023
Accepted: 25 July 2023
Published: 27 July 2023



## 1. Introduction

According to the January 2023 report from the UK Department of Business, Energy and Industrial Strategy [1], 18 of the 253 projects (7.1%) awaiting or under construction within the UK wind energy pipeline are offshore developments; however, these 18 projects account for 69.7% of the total approved pending windfarm capacity for the UK. Whilst it has been found that economies of scale are not present relative to total farm capacity for offshore developments, significant economies of scale can be attributed to increased individual turbine sizes [2]. It is logical, therefore, that the average offshore turbine size is increasing from 8.59 MW for those currently under construction, to 11.6 MW for those currently awaiting construction [1], and that the average turbine size will continue to increase as the industry progresses. It is noteworthy that this trend for larger turbine sizes is not present for onshore developments, with the average size of turbines in the onshore energy pipeline falling marginally from 3.75 MW in developments currently under construction, to 3.68 MW in developments awaiting construction [1].

Nejad et al. [3] estimate that 35% of the Levelised Cost of Electricity (LCOE) for offshore installations is in their operation and maintenance. As such, one of the principal opportunities for reducing the LCOE for offshore wind is through reducing offshore maintenance and repair. Traditional geared transmission systems are thought to fail within the region of 40% more often than direct-drive (DD) systems [4]. Further, as per a study of 1768 total years of offshore wind turbine operation, gearboxes were identified as the single most common source of failure resulting in major replacements per turbine per year, at 58.6% of major replacement category failures [5].

The removal of the gearbox in lieu of the direct coupling of the rotor shaft to the generator, in what is known as direct-drive (DD) generation, is therefore, touted as a low failure, high reliability alternative to conventional high-speed, geared turbines. Through the implementation of DD generators, other engineering challenges arise: The low rotational speeds characteristic of DD generators require vastly higher levels of torque in order to maintain the desired power outputs. This can be seen clearly in Equations (1) and (2), where $P$ is generator power (W) and the product of the generator's torque $T$ in Nm and its rotational velocity, $\omega$ (Rads/s); $R$ is the radial distance of the air gap from the centroid of the machine (m); $\sigma$ is the electrical shear stress (Pa); and $l$ is the 'stack' or magnet length (m).

$$P = T\omega, \tag{1}$$

$$T = 2\pi R^2 \sigma l, \tag{2}$$

This results in a requirement for large generator diameters, which consequently increases the structural mass and supporting requirements. Further, in order to avoid catastrophic structural failure, DD generators must maintain a strict air gap separating the rotor and stator, typically 1/1000th of its diameter, producing rigorous stiffness requirements. Minimising the structural mass of DD generators whilst maintaining these stiffness requirements has, therefore, been a key facet of DD wind turbine development and has received significant attention to date.

In [6], additive manufacturing in the production of a 5 MW permanent magnet direct-drive (PMDD) generator structure was explored to provide opportunities for lightweight design through the use of lattice structures and complex geometries inaccessible through traditional means. In [7], the dynamic performance of three distinct potential DD generator structures of a 3 MW machine are assessed, finding that conical structures have the potential to increase electrical operating ranges whilst minimising mass. The paper also finds potential for the use of stiffeners to manipulate natural frequencies and participation factors in the designer's favour, affording the opportunity to increase generator operating ranges without a significant increase in mass. The mass of a previously parametrically optimised 3 MW PMDD generator structure was further reduced through the use of topology optimisation within Ansys, in [8]. Accomplishing a total reduction of around 38% over the combined rotor and stator, the final design was found to satisfy the structural demands, whilst maintaining manufacturability.

Ref. [9] examines the use of hybrid additive manufacturing in the manufacture of complex lattice supporting structures in the design of a 5 MW PMDD generator. Triply periodic minimal surfaces, which are currently attracting interest in the matter of lightweighting, were shown to enable a maximum mass reduction for the generator of 34% through FEA and it was suggested scaling up to larger generator sizes was feasible. In [10], the NREL 15 MW Reference Turbine rotor structure was parametrically optimised, with the addition of holes and stiffeners, in a bid to reduce its mass whilst maximising the electrical operating range. Through Finite Element Analysis (FEA), within the Ansys Static Structural and Direct Optimisation modules, under Maxwell's electromagnetic torque and normal loads, and centripetal and in-plane gravitational forces, the addition of holes to the rotor structure led to a mass reduction of 20% and 34% under uniform and non-uniform loading, respectively.

Finally, in [11], a 3 MW PMDD conical rotor structure was optimised through parametric and topology optimisation techniques to satisfy dynamic operational conditions. The study highlighted the importance of designing PMDD generators to their dynamic operating conditions and modal responses, finding that the rotor mass requires to be increased 6.5 times over the typical corresponding static loading conditions when operating under worst-case-scenario loads. Additionally, the importance and influence of material choice on the structure's dynamic response was proven.

The effects of operating temperature on the structural stability of large-scale PMDD generators is, thus far, unknown. Whilst studies have been carried out analysing the

operating temperatures of DD wind turbine generators, the context on which they focus tends to be on the effects of temperature on the generator's power conversion efficiency and permanent magnet stability, as seen by the following studies.

The thermal behaviour of an 8 MW liquid-cooled PMDD wind turbine generator was investigated in [12], using FEA to predict the cooling performance of a liquid-cooled tooth-coil design, verified through a laboratory test. The performance of a high-density liquid-cooled 8 MW PMDD was analysed in [13], showing that liquid-cooled stator windings allow for a higher linear current density, maintain lower permanent magnet temperatures of around 50 °C, and winding temperatures of less than 80 °C. Ref. [14] details the optimisation of axial–radial ventilation spacers as a means to reduce the operating temperature rise within the generator, achieving a 3.9 °C temperature drop due to improved ventilation. A combined air-cooled heat exchanger and a liquid-cooled heat sink was investigated in [15] in order to provide a 2.5 MW PMDD wind turbine generator with adequate cooling whilst ambient temperatures increase. A radial, forced ventilation cooling structure was developed in [16], enabling the stator core and winding temperatures to be controlled to around 89 °C and 95 °C, respectively.

In [11], Jaen-Sola et al. incorporated operating temperature in their simulation and optimisation of a 3 MW PMDD rotor, introducing a constant, universal operating temperature of 55.69 °C to the rotor structure. Nevertheless, the extent of operating temperature's influence on the structural stability of larger, multimegawatt generators remains unclear. Further investigation as to its contribution to deformation, as well as the individual contributions of the thus-far established loading parameters would provide a clearer picture as to the forces that ought to be designed to. Considering also the trend of ever-increasing generator sizes, this paper therefore, sets out to determine the influence of each operating parameter on the 15 MW NREL Reference Wind Turbine generator rotor structure.

Figure 1 details the workflow applied in this paper:

1 An initial structural analysis of the rotor under established static operating conditions;
1 Optimisation of the rotor according to those conditions;
1 Subsequent analysis of the optimised rotor, with the inclusion of the generator's operating temperature added to the simulation, finding that deformation was consequentially increased beyond its limits;
2 Simultaneous costing and environmental impact analyses of the optimised structure, accounting for material use, energy consumed, and $CO_2$ emitted through manufacturing and transport, as well as energy expenditure through end-of-life processes;
3 A parameter study of the operating loads to evaluate the influence of each load on structural integrity as changes to the rotor geometries are made towards optimisation.

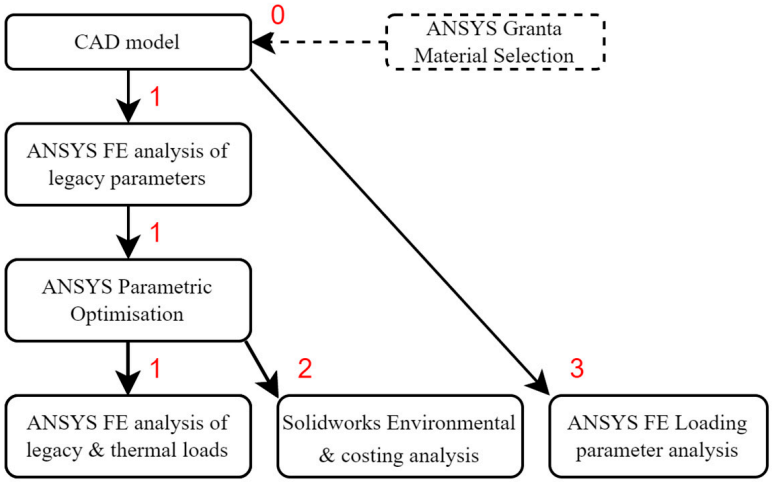


**Figure 1.** Project flowchart, including material selection process detailed in [17].

This paper builds on the findings of [17] wherein a systematic material selection process was devised for the NREL 15 MW PMDD Reference Wind Turbine rotor structure. The resulting candidate material was used for all simulations carried out through this paper, and as such, the material selection process was included in the workflow chart in Figure 1, where it is represented by a dashed textbox and referred to as 'Ansys Granta Material Selection'.

*NREL 15 MW Reference Wind Turbine*

The National Renewable Energy Laboratory's 15 MW Reference Turbine [18] seen in Figure 2, allows for collaborative research and innovation in turbine design at a scale suitable for the current offshore wind industry and shall therefore function as the medium for the research carried out through this paper.

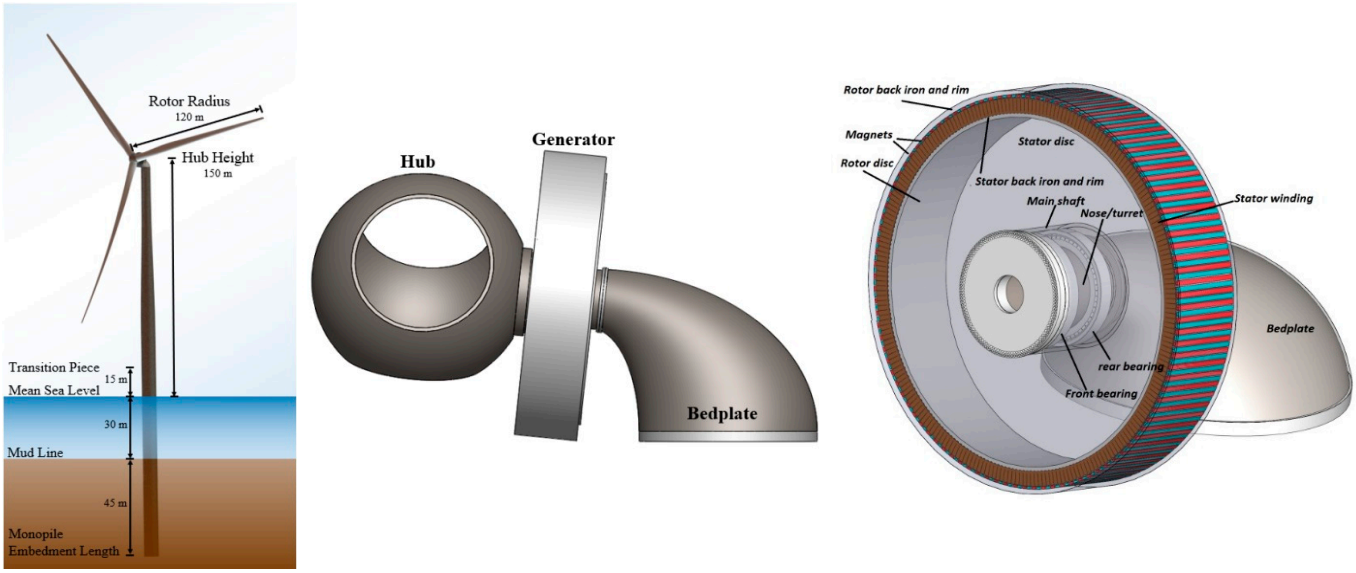


**(a)** **(b)** **(c)**

**Figure 2.** (**a**) The 15MW NREL Reference Wind Turbine; (**b**) hub, generator and bedplate assembly; (**c**) direct-drive generator detail, including active and inactive materials [19].

Moreover, CAD models of the generator are available through the turbine's GitHub repository [19]. This reference turbine incorporates an IEC Class 1B, direct-drive, outer-rotor, radial-flux, permanent-magnet synchronous machine, with an air gap diameter of 10.53 m, and a stack length of 2.17 m. This resource also assumes at least 50% of the generator's mass is comprised of inactive material.

## 2. Materials and Methods

In designing a direct-drive generator supporting structure there are several key loads that must be considered. These are presented in Section 2.3 and are used, amongst others, in papers [9,10,20]. Through an initial structural analysis, this paper first finds that the unaltered NREL 15 MW Reference Wind Turbine rotor does not comply with the structural loading requirements imposed on it through normal operation. Novel to this paper, operating temperature was accounted for within the subsequent structural analysis and was found to have catastrophic effects on the rotor's structural integrity, thereby establishing that the inclusion through the design stages of this thus far unaccounted-for operating parameter is imperative to ensure structural integrity. Likewise unique to this paper, Section 3.5 details an analysis of the effects of each individual loading parameter on the structural integrity of the rotor, which further affirms operating temperature as a primary contributor to deformation as the structure is scaled up towards optimisation. Moreover, the quantification and comparison of the rotor's environmental and financial performances,

pre and post parameter optimisation, which are presented in Sections 3.3 and 3.4, are also unique to this paper.

### *2.1. Rotor Substructure Topologies*

As detailed in [20], there are several different rotor substructure topologies, which can be defined by the manner in which they provide radial support to the active rotor components. Typical geometries include simple disks which can be internally or end mounted, conically supported such as the example detailed in [11], as well as internal or end mounted spokes and support arms. Additionally, various rib stiffeners can be employed. These substructures are displayed in Figure 3.

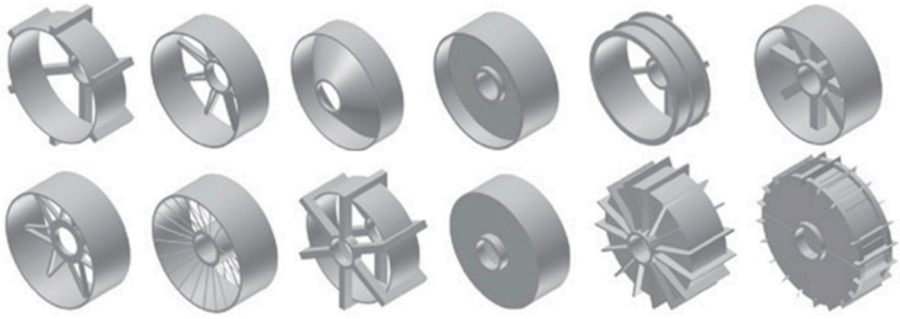

**Figure 3.** Rotor supporting structure geometries [11].

The 15 MW Reference Wind Turbine rotor, used in this paper, is a simple, end-mounted disk supported structure.

### *2.2. Deflection Modes*

As Figure 4 shows, deformation of the rotor can manifest in several ways. Accordingly, air gap closure and hence, as per [8], ultimate structural failure can occur due to:

(a) Mode 0: Relative radial expansion of the inner stator or radial compression of the outer rotor.
(b) Mode 1: Relative displacement of the rotor and stator.
(c) Mode 2: Distortion of either or both stator and rotor surfaces into ellipses.
(d) Mode n: Distortion of either surface into ripples, with n number of peaks.

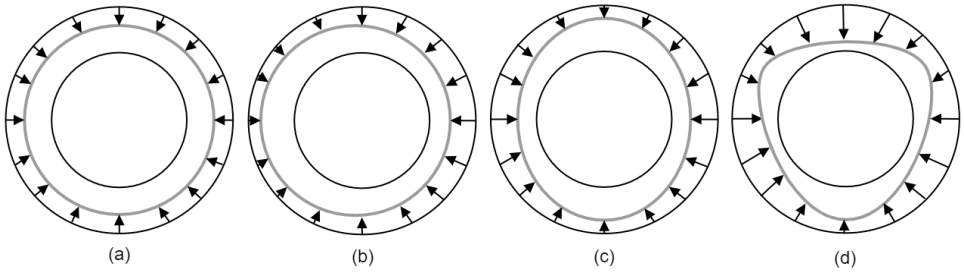


**Figure 4.** Outer rotor deformation modes: (**a**) Mode 0, radial expansion ($\delta_{(\theta)} = \overline{\delta}$); (**b**) Mode 1, displacement $\delta_{(\theta)} = \overline{\delta} + \delta_{\Delta}\ sin(\theta - \varphi)$; (**c**) Mode 2, ellipse distortion $\delta_{(\theta)} = \overline{\delta} + \delta_{\Delta}\ sin(2(\theta - \varphi))$; (**d**) Mode 3, ripple distortion $\delta_{(\theta)} = \overline{\delta} + \delta_{\Delta} sin(3(\theta - \varphi))$.

In Figure 4, $\delta_{(\theta)}$ is the local variation in air gap clearance in meters at angle $\theta$, around the generator circumference, $\overline{\delta}$ is the mean radial deflection (m), $\delta_{\Delta}$ is the variable deflection (m), and $\varphi$ is the phase angle of the component in degrees.

### *2.3. Rotor Operating Loads*

There naturally exist several forces acting upon the rotor structure which must be accounted for within the design process in order to ensure the integrity of the machine is

uncompromised during operation. Normal, or Maxwell stress is largest of the operating loads within the generator and is the result of the attraction between the permanent magnets mounted on the rotor and the magnetism produced by components of the stator. The following formula can be used to calculate the magnetic loading stress distribution through the circumference of the rotor under Modes 0, 1, 2, and 3.

$$\sigma_{PM}(\theta, \bar{\delta}, \delta_\Delta) = \frac{\hat{F}_{PM}^2 cos^2(p\theta)\mu_0}{2\left(g + \frac{h_m}{\mu_r} - \bar{\delta}\right)^2}\left[1 + \frac{2\delta_\Delta \sin(n\theta)}{g + \frac{h_m}{\mu_r} - \bar{\delta}} + \frac{{\delta_\Delta}^2 sin^2(n\theta)}{\left(g + \frac{h_m}{\mu_r} - \bar{\delta}\right)^2}\right] \approx \frac{\hat{F}_{PM}^2}{4\left(g + \frac{h_m}{\mu_r} - \bar{\delta}\right)^2}\left[1 + \frac{2\delta_\Delta sin(n\theta)}{g + \frac{h_m}{\mu_r} - \bar{\delta}} + \frac{{\delta_\Delta}^2 sin^2(n\theta)}{\left(g + \frac{h_m}{\mu_r} - \bar{\delta}\right)^2}\right] \quad (3)$$

where $\sigma_{PM}$ is the magnetic or normal component of the Maxwell stress (Pa), $\theta$ is the pitch angle, $\bar{\delta}$ is the mean radial deflection (m), and $\delta_\Delta$ is the variable deflection (m), the combination of which produces the total deflection. $\hat{F}$ corresponds to the magnetomotive force produced by the rotor field and the current in the armature windings (N); $p$ is the number of generator pole pairs; $\mu_0$ is the permeability of free space (H/m); $n$ is the mode of deflection; $g$ is the nominal air gap clearance (m); $h_m$ is the magnet height from the rotor surface (m); and $\mu_r$ is the relative permeability. This equation facilitates estimating the local magnetic stress through the rotor's circumference, which is produced under different deflection modes through a combination of variable deflection and the radial mean deflection. The total deflection under each mode can be obtained, and hence Equation (3) can be used to calculate stress under each mode [11].

The localised stress force experienced by the rotor is visualised below, in Figure 5.

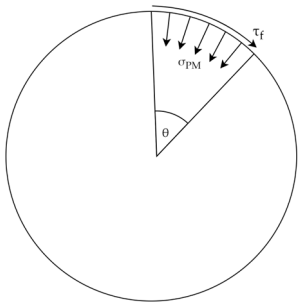


**Figure 5.** Local electromagnetic stress ($\sigma_{PM}$) and torque ($\tau_f$) on the rotor, over a partial circumference ($\theta$).

Shear stresses are generated on the rotor surface as mechanical energy is converted into electrical energy due to the interaction between the rotor's magnetic field and the current in the stator windings. The shear force on the rotor is opposed by an equal force on the stator under steady state conditions. Gravitational loads are, of course, present at all times but are of greatest concern during transport and installation, where the large diameters and masses required of multi-megawatt generators prohibit transportation by road and often require transportation in segments. As a rotating mass, the rotor is subject to centrifugal forces, although owing to their low-speed operation, these forces are comparatively small. Lastly, through the dissipation of heat arising due to copper losses in the stator windings and hysteresis losses in the rotor's permanent magnets, elevated working temperatures can cause thermal expansion of the rotor supporting structure during operation.

### *2.4. Facilitation of Simulation, Optimsation and Performance Analysis*

Ansys [21] is a multidisciplinary analysis package that enables the simulation of mechanical, fluid dynamic and thermodynamic models. Finite Element Method analysis of the rotor was carried out within the Static Structural analysis module from the workbench. Parametric optimisation of the rotor structure was then performed in the Direct Optimisation module using the Adaptive Multiple-Objective method to vary the thicknesses of both the cylinder and disk walls in order to reduce the maximum total deformation experienced

by the rotor under the expected operating conditions with the minimal necessary mass increase. The optimisation method utilises a Non-Dominated, Sorted Genetic Algorithm, and outputs are only calculated if the geometry is valid, i.e., continuous and manufacturable.

SolidWorks was used first to import and link the original CAD part directly into Ansys through Ansys' CAD plug-in, such that changes to the rotor's shape through parametric optimisation were implemented in real time in the respective SolidWorks part. This then allowed the Sustainability software integrated in SolidWorks to evaluate the environmental impact of the optimised rotor geometry for factors such as carbon footprint, energy consumption, air acidification and water eutrophication (the enrichment of water with specific minerals and nutrients that can lead to negative side effects such as algal blooms) over its lifetime [22]. Electricity, natural gas, and scrap rate during manufacturing processes can be specified, along with transportation methods and distances to installation sites. The costing tool integrated in SolidWorks [23] was then used to calculate the cost of manufacture for the rotor geometries through the known costs of the material, as well as the cost and time requirements to cast the part and the cost of the required mold.

### *2.5. Finite Element Analysis*

Following the metal selection process devised in a previous output [17], in which successive filters for mechanical and thermal properties, manufacturing process capabilities and material unit price were implemented, 'Carbon Steel SA216 (Type WCC), Cast Annealed' was selected and assigned to the rotor structure, resulting in a mass of 122.5 tonnes for the unaltered geometry. A tetrahedral mesh with adaptive sizing was generated in the mesh independence study, where mesh density was increased through a 20 mm step reduction in the mesh element size from 260 mm, until stabilisation of the results at a mesh size of 140 mm.

The following four loads were imposed on the rotor and can be seen in Figure 6. Accounting for the rotor's tilt angle of 6°, and in keeping with the process followed in [10], an in-plane acceleration due to gravity (g) of 9.76 $ms^{-2}$ was applied, along with a rotational velocity ($\omega$) of 0.79 $rads^{-1}$ to account for centrifugal forces. To represent Maxwell's electromagnetic stress ($\sigma_{PM}$), a static radial compression load of 447 kPa was applied uniformly and normally to the inner cylinder surface. A torque ($\tau_f$) of 21 MNm was applied uniformly and tangentially to the inner cylinder surface. Additionally, a fixed weight of 46,021 kg was applied uniformly to the inner cylinder surface to represent the mass of the rotor yoke and magnets, as calculated in [10], and a fixed support was applied to the inner cylinder face of the disk. The environment temperature was set to 22 °C.

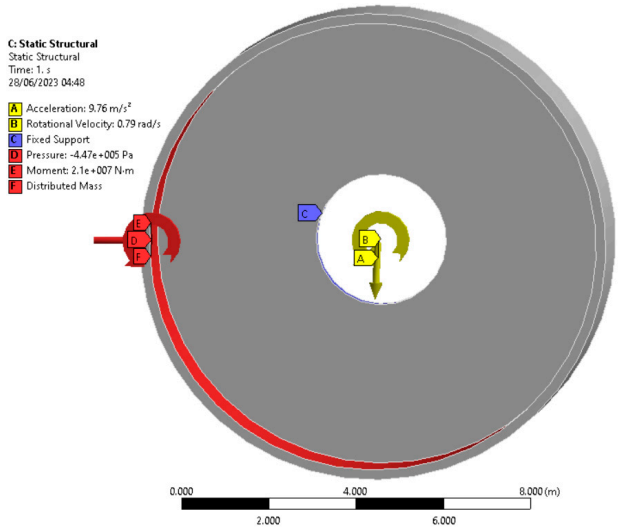


**Figure 6.** Loads applied to the 15MW RWT rotor.

The rotor criteria dictate that the maximum permissible Von Mises stress experienced by the rotor is 200 MPa (note that the NREL 15 MW machine comprises an outer rotor and that the normal load caused by the magnetic attraction generates a compressive stress), and the ultimate limit for the total deformation of the rotor is 20% of the total air gap clearance, equating to 2.03 mm. Figure 7 shows the generator assembly, including the stator teeth and rotor magnets, and the airgap that separates them.

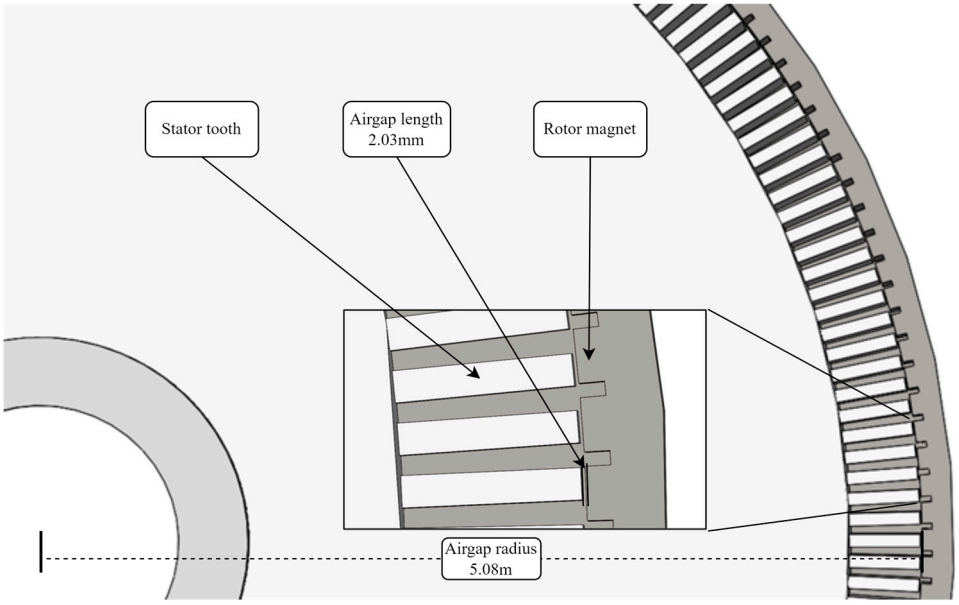


**Figure 7.** Electrical generator assembly highlighting dimensions and airgap.

### *2.6. Paramteric Optimisation and Further Analysis*

Under objectives and constraints, the total deformation maximum was set to minimise, with a target of 0.99 mm within an upper bound constraint of 1 mm and a tolerance of 0.1 mm. The rotor mass was set to minimise without target or constraint. The rotor's cylinder and disk thicknesses were then configured within lower and upper bounds, which the programme uses to generate candidate points accordingly. These were increased incrementally as the programme trended towards deformation and stress goals, to final upper and lower bounds of 450 and 410 mm, respectively, for the disk thickness, and 10,700 and 10,780 mm, respectively, for the outer cylinder diameter.

Thermostructural analysis was then carried out on both the unaltered and optimised geometries by linking the previous Static Structural module with a Steady-State Thermal module. In accordance with the aforementioned study from Jaen-Sola et al. [11], a constant universal body temperature of 55.69 °C (~56 °C) was additionally applied to the rotor. This figure was extracted from SCADA data of an offshore 7 MW machine that were made available by the Offshore Renewable Energy Catapult [24]. The environment temperature was unchanged at 22 °C.

Finally, a parametric loading study was carried out, again with linked Static Structural and Steady-State Thermal modules. To clearly distinguish the effects of the rotor and cylinder wall thicknesses on deformation, and in contrast to the algorithm employed in optimisation, these thicknesses were increased linearly by steps of 30 mm, both individually and collectively. For each respective geometry, each operating load was simulated separately such that its influence on structural deformation and stress could be tracked as the wall thicknesses were increased to meet the limits. Lastly, there are two additional considerations. The first is that all the thus-far established loading parameters—gravity, normal and torque stresses, centrifugal forces and fixed weight of magnets, etc., (hereafter referred to as the *'Legacy'* loading parameters)—were simulated simultaneously. Secondly, operating temperature was included together with all the legacy parameters. In all, 6 itera-

tions were run from the baseline unoptimised rotor, resulting in 19 separate geometries, each simulated for 7 input parameter configurations.

## 3. Results

In this section, we first present the results of the mesh independence study and the mesh produced for the parameter optimised rotor geometry. The optimised rotor structure is then compared against the unmodified structure for its structural performance under static, legacy operating conditions, and then with the addition of operating temperature on the structure. Next, the optimised rotor's expected environmental and financial impact are given. Lastly, the findings of operating parameter study are presented.

### *3.1. Mesh Independence Study*

A high density, tetrahedral mesh with an element size of 140 mm was generated through the mesh independence study, resulting in a total of 65,289 nodes and 32,397 elements for the unaltered rotor geometry. The mesh of the parameter optimised rotor geometry consisted of 91,279 nodes and 51,569 elements.

### *3.2. Finite Element Analysis and Rotor Optimisation*

As shown in Table 1, under the 'legacy' loading conditions it was found that the unaltered geometry experiences a maximum Von Mises stress of 87.49 MPa and a total deformation of 25.97 mm. In order for the optimised design to meet constraints, a disk thickness increase of ~335 mm and cylinder thickness of ~115 mm over the baseline is required, resulting in the optimised rotor weighing over three times the starting mass, at 398,019 kg. This increase is considerable, and although the structure has been optimised parametrically, considering the implication the added weight has on the generator's supporting structures, further optimisation through additional techniques is a necessary step in future work.

**Table 1.** Parameter optimisation and thermostructural analysis results.

| Description | Original NREL | Parameter Optimised | Limits |
|---|---|---|---|
| Disk thickness (mm) | 82.21 | 416.18 | - |
| Cylinder thickness (mm) | 129.06 | 224.32 | - |
| Mass (kg) | $1.2255 \times 10^5$ | $3.9802 \times 10^5$ | - |
| Structural Analysis results | | | |
| Max equivalent Von Mises stress (MPa) | 87.49 | 13.07 | 200 |
| Max total deformation (mm) | 25.97 | 0.991 | 1 (2.03) |
| Thermostructural Analysis results | | | |
| Max equivalent Von Mises stress (MPa) | 220.07 | 172.04 | 200 |
| Max total deformation (mm) | 26.78 | 2.15 | 1 (2.03) |

For the unoptimised rotor, when accounting for the thermal loads attributable to the operating temperature of ~56 °C, total deformation of the structure increases 3.1% to 26.78 mm. Deformation of the parameter optimised rotor, accounting for operating temperature, increases to 2.15 mm, from 0.99 mm, an increase of ~117%. Alarmingly, despite the safeguard provided by the stricter imposed deformation limit of 1 mm, when accounting for operating temperature, the rotor structure is found to be outside the ultimate deformation limit of 2.03 mm.

Figure 8a makes clear the dominance of thermal expansion in the deformation pattern over the disk compared with the deformation pattern in Figure 8b, where thermal operating

parameters are not considered. Figure 8a shows the eccentric deformation pattern arising from gravity and the tilt imposed on the generator, whereas no such eccentricity is present in the thermal simulation in Figure 8b.

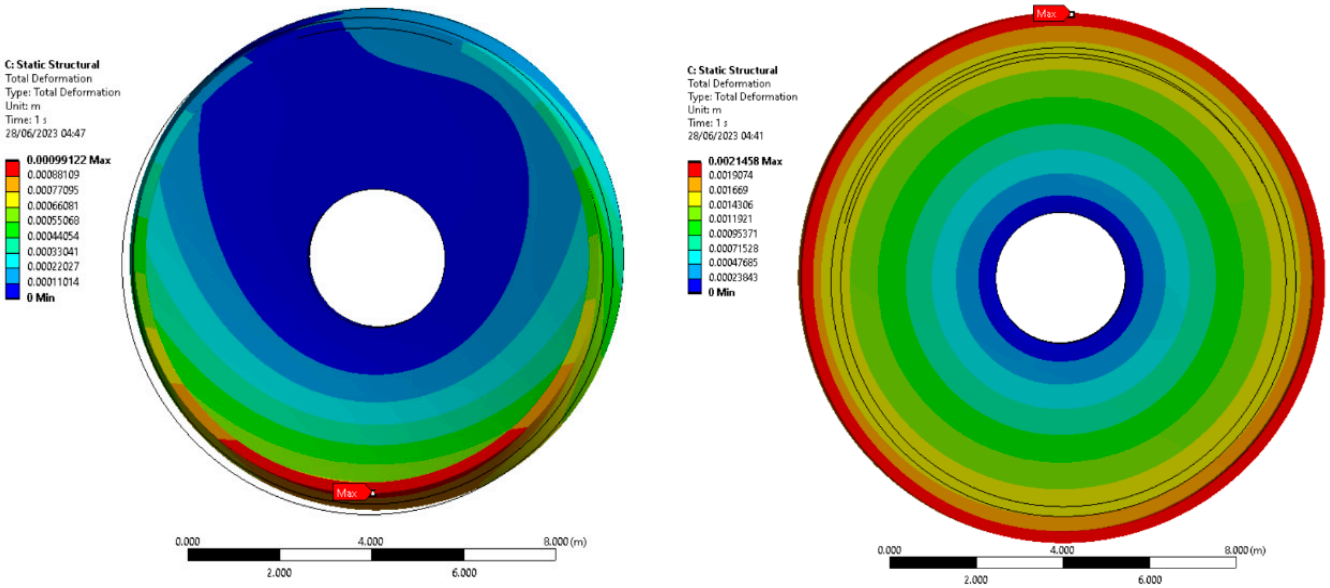


(**a**) (**b**)

**Figure 8.** (**a**) Total deformation of the parameter optimised rotor without consideration of operating temperature. (**b**) Total deformation of the parameter optimised rotor accounting for an operating temperature of 56°C.

### *3.3. Environmental Performance*

The SolidWorks Sustainability tool uses the environmental Life Cycle Analysis (LCA) database GaBi [25], a leading LCA software tool developed by Sphera. This was used to estimate the environmental impact of the unaltered and optimised rotor geometries, according to their manufacturing methods and material use. The SolidWorks library includes a cast carbon steel which closely resembles the material properties of the SA216 (Type WCC, cast) steel used in this analysis in all relative fields aside from thermal conductivity. As thermal conductivity has an influence on the energy consumed during the casting process, it should, therefore, be noted that this material cannot directly represent the SA216 (Type WCC, cast) steel.

It should be noted that the mass of the rotor mounting shaft was added to the rotor design through the environmental and costing analyses to allow for direct comparison with future designs which may be enabled by its inclusion, and therefore, all figures reflect the addition of this part. The material of the mounting shaft is identical to the rotor, as it was presumed that the rotor and its shaft are caste as one part through hybrid, sand-mold casting.

As shown in Table 2, SolidWorks estimates that the parametrically optimised rotor structure produces 291 tonnes of carbon dioxide emissions. According to a study of steelmaking in China [26], the production of one tonne of steel would result in the emission of 4.4 tonnes of $CO_2$ and $CO_2$ equivalents, which would equate to 1752 tonnes of $CO_2$ emissions in the case of the rotor. The discrepancy in this figure may be due in part to a more in-depth analysis of the requirements for steelmaking than SolidWorks allows, or a higher embedded $CO_2$ cost due to production in China as opposed to Europe.

**Table 2.** Environmental impact of rotor design.

| | Energy (Tera Joules) | Carbon Dioxide (Tonnes) | Water (Mega Litres) |
|---|---|---|---|
| Unaltered Rotor | 1.63 | 98.22 | 3.76 |
| Optimised Rotor | 4.84 | 291.04 | 11.13 |

SolidWorks also estimates the use of 11.1 million litres of water in the production of the rotor structure. This is consistent with the literature, where [27] finds total water lifecycle withdrawal, water consumption and water discharge rates of 14.93 t, 5.9 t and 9.23 t, respectively, per tonne of steel produced, therefore finding a total water usage of 30.06 t per tonne of steel. Here, water lifecycle withdrawal refers to the total amount of water withdrawn from surface, ground or other sources, while water consumption refers to the volume of water permanently lost from the source due to evaporation, or consumption by processes, humans, plants or animals, and discharge refers to water effluents returned to the environment after use which may contain contaminants or be at different temperatures to the environment it is returned to. Applying this figure to the total rotor structure mass of 398.2 tonnes would require 11.97 million litres of water.

An estimated total energy requirement of 4.84 TJ or 1344.44 MWh is given by SolidWorks for the production of the rotor structure, which is in agreement with the figure given in Table 16—'Comparison of theoretical minimum energy requirements derived here with real world energy use' on page 329 of [28] for the observed energy use in an efficient blast furnace at 11.72 GJ per tonne, equating to a total of 4.67 TJ.

SolidWorks Sustainability suggests relative percentages of environmental impact in other areas such as transport, end-of-life impact, and material sourcing. While it cannot be used to directly ascertain accurate values for the choice material due to the aforementioned difference in thermal conductivity of the choice material and available library material, it can help indicate the potential environmental impact of each parameter setting between designs for that given library material.

Figure 9 shows that the carbon dioxide emissions produced, and energy and water consumed in product transport and end-of-life processes were consistent as a percentage of manufacturing impacts. SolidWorks Sustainability does not provide a full breakdown of water usage, such as eutrophication due to transport and end-of-life processes but does include water consumed as engine coolant and operations by freight handlers when evaluating the impact of these parts of the supply chain.

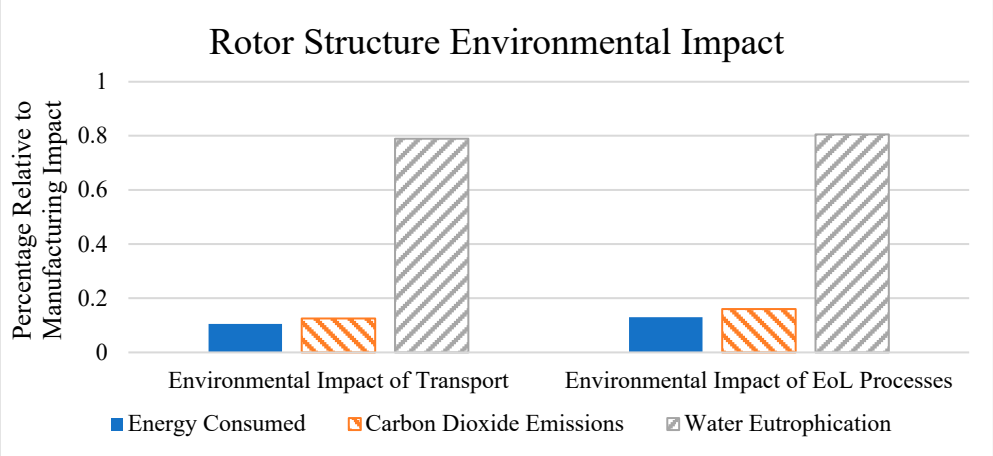


**Figure 9.** Environmental impact of rotor structure.

Carbon dioxide emitted during transport was found to account for 12% of the manufacturing emissions, and emissions during end-of-life processes were found to be 16%.

Energy consumed for transport was found to be 11% of manufacturing energy consumption, and end-of-life processes consumed 13%. Water eutrophication due to transport was found to average 81% of eutrophication due to manufacturing, and 80.5% due to end-of-life processes.

### *3.4. Costing Analysis*

Table 3 presents the total production costs of both the optimised rotor and the unmodified, NREL Reference Turbine rotor, broken down into costs accrued in manufacturing alone, and additional costs accounted for within financial impact.

**Table 3.** Rotor manufacturing costs.

| | | **Unoptimised Rotor** | **Parameter Optimised Rotor** |
|---|---|---|---|
| Manufacturing cost | GBP (USD) | 99,100 (123,400) | 296,500 (369,200) |
| Change from original | % | - | +199.2 |
| Financial impact | GBP (USD) | 59,100 (73,600) | 196,100 (244,200) |
| Change from original | % | - | +231.7 |
| Total | GBP (USD) | 158,200 (197,000) | 492,500 (613,300) |
| Change from original | % | - | +211.3 |

The rotor's financial impact is determined by the SolidWorks Sustainability tool and includes manufacturing energy costs, supply costs additional to raw material cost, transport, and end-of-life costs. This parameter again serves as an indication and estimation of the cost and is included to consider additional financial impacts not accounted for by the costing tool and template. These costs are estimated using an assumed labour cost of USD 50/h, a machine rate of USD 12/h and a requirement for a 10% sand replenishment rate per casting. The mean value of the material per kilogram is 0.84 USD/kg within the Ansys Granta material database used in the material selection process devised in [17], and the exchange rate used at the time of writing was 1.00 USD:0.803 GBP.

The costing analysis results show that provided the manufacturing processes remain unchanged with the changes to the rotor geometry, in order to produce a rotor design compliant with the performance limits of 1.00 mm deflection and 200 GPa stress under legacy conditions, the total part costs would increase by 334,267.1 GBP, an increase of 211.3% compared with the original NREL 15 MW Reference Turbine rotor.

### *3.5. Operating Parameter Study*

Of the 'legacy' loads, centrifugal forces (Figure 10a) were found to have the least influence on the structure, producing a maximum deformation of 0.017 mm in the case of the unaltered rotor structure and decreasing as both the cylinder and disk thicknesses were increased.

Shear stresses resulted in a deformation of 0.574 mm at the baseline and decreased as disk thickness was increased to 0.187 mm of deflection by the sixth iteration, as seen in Figure 10b. When increasing cylinder thickness, deformation increased marginally to 0.585 mm. Interestingly, as both the disk and cylinder thicknesses were increased, deformation decreased at a marginally faster rate than the disk alone, starting from the second iteration. This suggests the decrease due to disk optimisation outweighs the increase due to increased cylinder mass and indicates parametric optimisation can be achieved faster and more efficiently by increasing disk and cylinder thicknesses simultaneously, rather than following an individual approach.

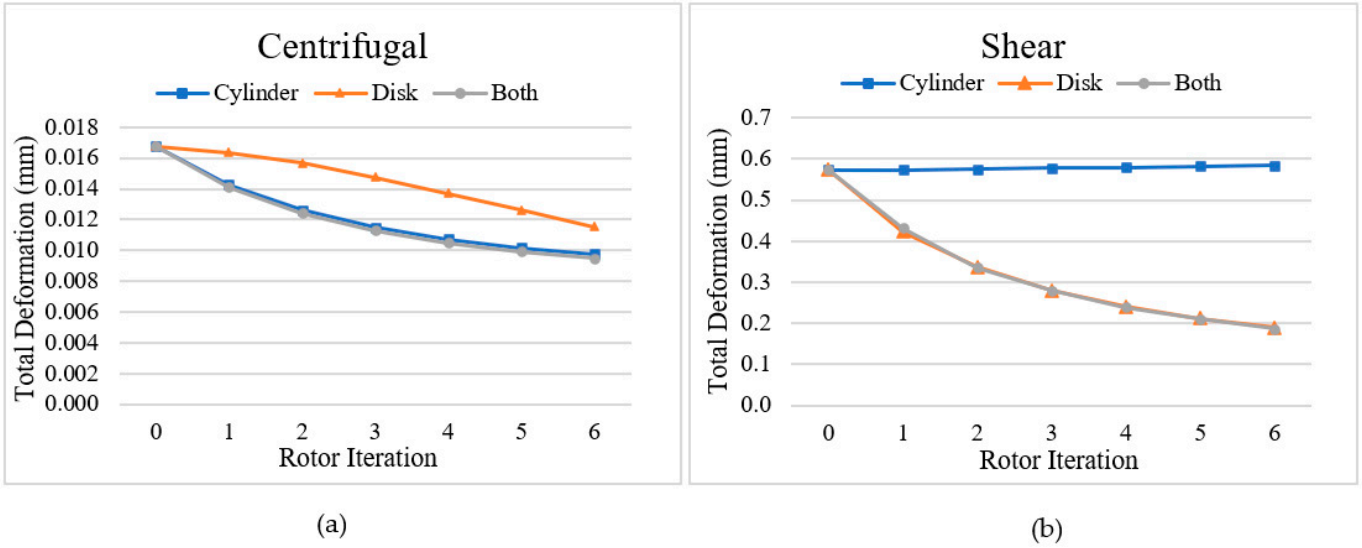


**Figure 10.** (**a**) Centrifugal deformation. (**b**) Shear stress deformation.

Deformation due to normal stresses was found to reduce with increases to both disk and cylinder thicknesses, with the cylinder providing the greatest source of relief, reducing deformation from the baseline of 1.515 mm to 0.469 mm versus the disk deformation of 1.031 mm for the sixth iteration (Figure 11b). More obviously, increasing the thickness of both together resulted in the lowest deformation due to normal stresses, with a value of 0.454 mm by the sixth iteration.

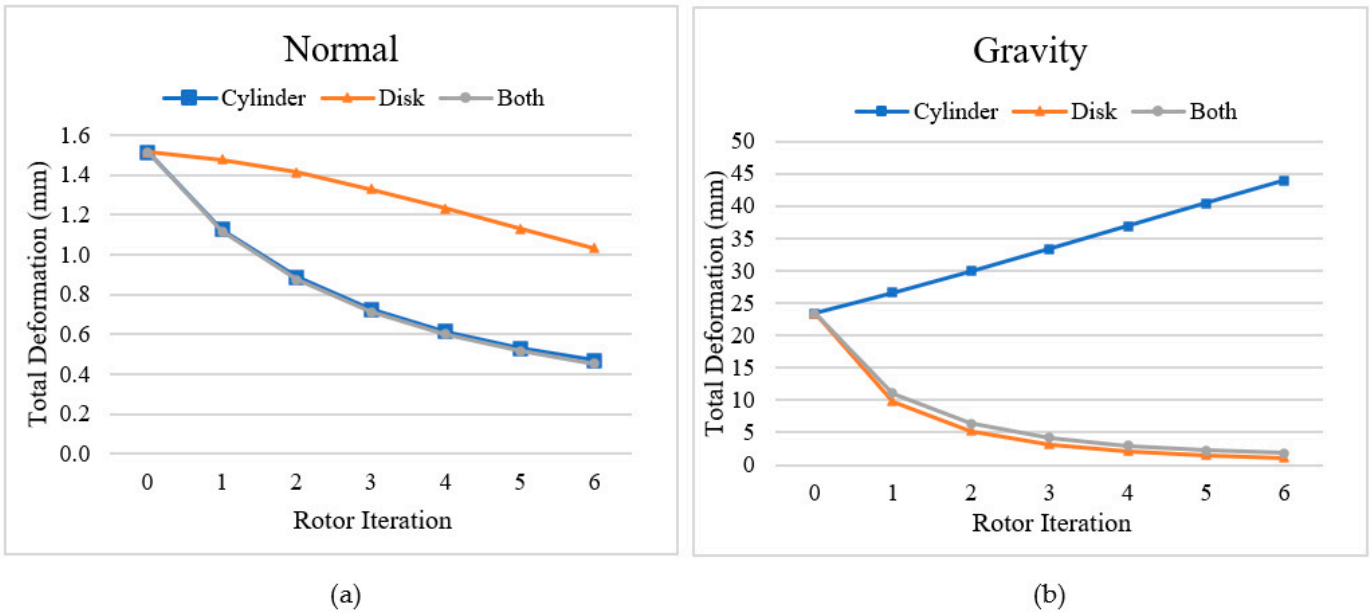


**Figure 11.** (**a**) Normal stress deformation. (**b**) Gravitational deformation.

Gravity had by far the biggest influence on deformation of the 'legacy' loads initially, causing 23.4 mm deflection on the unaltered rotor geometry. As seen in Figure 11b, this is reduced drastically by increasing disk wall thicknesses to 1.105 mm by the sixth iteration. The opposite is true of the cylinder wall thickness, which increases to 44 mm of deflection at the sixth iteration as a result of the vastly increased mass of the cylinder being increasingly insufficiently supported by the disk. As expected, these effects are counteracted when the thicknesses of both the disk and the cylinder are increased simultaneously, with a maximum deformation of 1.802 mm by the final iteration. For the combined simulation of the legacy

loads, the effects of gravity were again dominant in the cylinder only study, as depicted in Figure 12a. The deformation increased compared with the study of gravity alone, however, with a total deformation of 44.458 mm for the sixth iteration. When increasing the thickness of the disk only, the deformation decreased from the initial 24.895 mm to 2.130 mm. The combined increase to the disk and cylinder thicknesses reduced total deformation to 1.105 mm, which is well within the 2.03 mm limit.

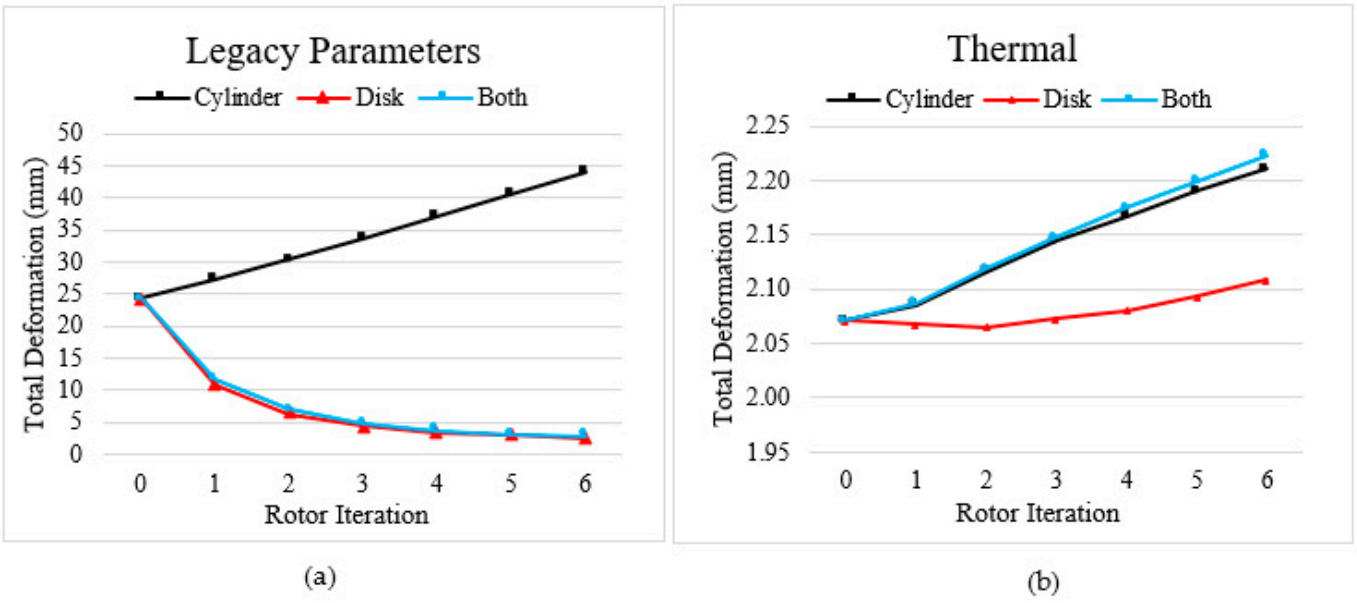


**Figure 12.** (**a**) Deformation under 'legacy' parameter loads. (**b**) Deformation due to thermal loads.

The operating temperature of ~56 °C produced a deformation of 2.071 mm on the unoptimised structure, and whilst this does exceed the deformation limit, it was initially presumed to be manageable through optimisation. It was found, however, that increases to both the cylinder and the disk thicknesses resulted in increasing levels of thermal deformation to 2.211 mm and 2.108 mm, respectively, and an increase to 2.223 mm when both the cylinder and disk were increased simultaneously, as shown in Figure 12b.

These results are near linear for the cylinder; however, the initial two iterations show a marginal decrease in thermal deformation as the disk thickness is increased.

Thermal deformation alone was shown to have a strong linear correlation with the mass of the rotor, with a coefficient of determination ($R^2$) of 0.9962, as both the disk and cylinder thicknesses were increased, as shown in Figure 13, corroborating the necessity of minimising rotor mass.

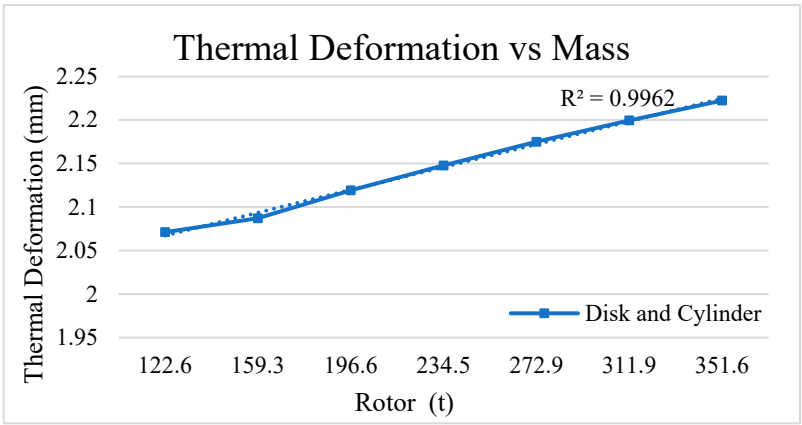


**Figure 13.** Thermal deformation vs. rotor mass.

When consolidating all input loads (Figure 14a), the deformation was reduced as the disk thickness increased, and as with the case of the legacy loading parameters in Figure 12b, the increase in cylinder thickness alone resulted in increased deformation.

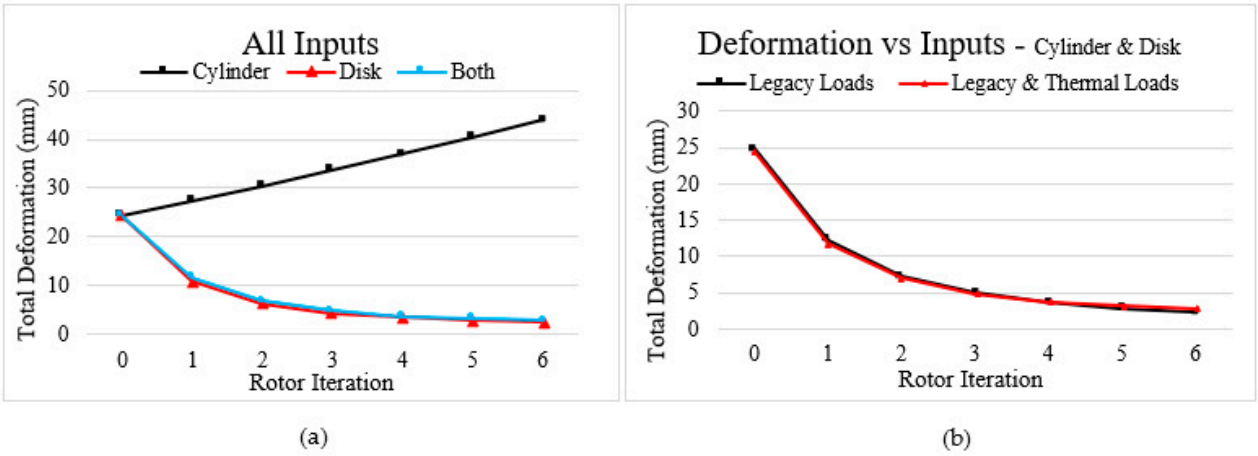


**Figure 14.** (**a**) Deformation due to all loads. (**b**) Deformation of the disk and cylinder combined.

In comparing the legacy parameter case against the inclusion of operating temperature in Figure 14b, deformation was initially found to be lower with the inclusion of operating temperature than without, at 24.303 mm versus 24.895 mm, respectively, for the unchanged geometry. This difference decreased for the following three iterations, while at the fourth iteration, deformation was increased by the inclusion of operating temperature. By the sixth iteration, total deformation was some 0.58 mm greater with the inclusion of operating temperature compared with the simulation without.

It was found that increasing only the disk thickness reproduced the reversal whereby the inclusion of operating temperature led to higher levels of deformation in the fourth iteration geometry than when excluding thermal effects. This trend was also observed for the cylinder, albeit a much greater increase in the cylinder thickness would be required before the deformation produced in the simulation of all the loads including operating temperature would be greater than that produced in the simulation of the legacy loads for the cylinder alone. Notable too were the effects of the inclusion of operating temperature on the rotor's Von Mises stress levels, with the maximum Von Mises stress of 21.65 MPa for the model with both disk and cylinder thicknesses increased when operating temperature was not considered, versus 171.6 MPa when thermal loads are accounted for, as seen in Figure 15.

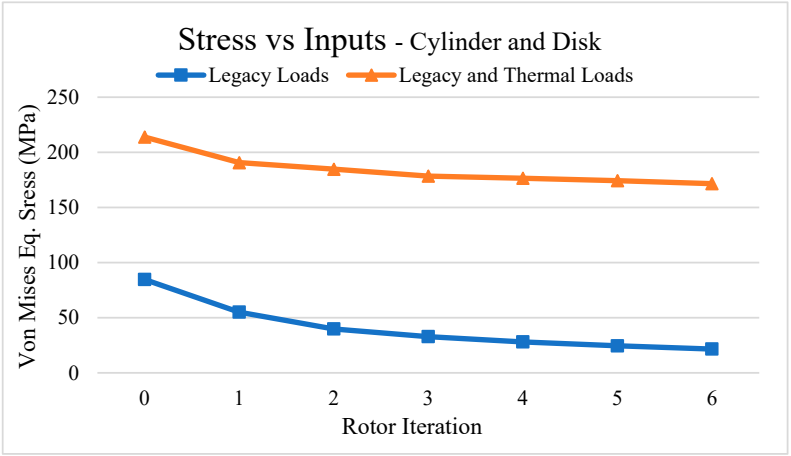


**Figure 15.** Maximum Von Mises Stress.

The raw data obtained from the operating parameter study is available in Appendix A, presented in Tables A1 and A2.

## 4. Discussion

The results obtained from the initial FEA of the legacy loads agree with previous studies and are supported by the mesh independence study. Carried out through parametric optimisation alone, however, the optimisation of the rotor necessary to ensure its structural integrity was found to contribute an increase of 398,019 kg to the rotor mass. This was concluded to be unfeasible without further optimisation. It is prohibitive due both to excessive financial and environmental costs accrued in production and to the increased mass of the rotor contributing to thermal deformation.

The results obtained when including operating temperature in the simulation of the optimised rotor indicate the importance of this factor as direct-drive generator structures are scaled up. In the Finite Element Analysis of the optimised rotor, the maximum total deformation limit was breached despite incorporating a significant margin for excess through the stricter imposed limit of 1 mm deflection. A notable caveat is that the additional mass of the rotor required to reduce deformation from compliance with the 2.03 mm limit to the stricter limit under the legacy loading scenario, will in and of itself contribute detrimentally to the increase in thermal deformation, as is proven by the operating parameter study.

A novel contribution of this paper is that the operating parameter study establishes the requirement to account for operating temperature in the design and optimisation of multi-megawatt direct-drive generator structures of this size. In contrast, the impact of centrifugal forces was proven minimal in its contribution to total deformation, and in instances where computational resources are scarce, the exclusion of centrifugal forces may be appropriate.

Through the environmental impact analysis, estimates of the rotor's environmental impact attributed to its manufacture were found to be significant, with 11.1 million litres of water used during the production processes, which is equivalent to over four Olympic swimming pools. Further, to offset the energy requirements of production, over 37 days of operation at the rated power output would be required to offset the energy requirements of manufacturing the rotor structure alone.

The results presented through this study demonstrate that for a turbine of this scale, parameter optimisation of the standard form, disk-supported rotor structure is inadequate when accounting for rotor operating temperatures and when considering both the financial and environmental costs attributed to the rotor supporting structure. The mass increase necessary in order to achieve structural stability is prohibitively large when other optimisation techniques are not considered.

## 5. Conclusions

To establish the importance of each operating load on the integrity of large-scale direct-drive electrical generator structures, the NREL 15 MW rotor structure was first optimised parametrically under the 'legacy' operating loads accepted in the literature.

An operating temperature of ~56 °C, which was taken from SCADA data of an offshore wind turbine, was subsequently introduced to the structural simulation and was found to dramatically increase total maximum deformation, from 0.99 mm to 2.15 mm, breaching deformation limits.

Further analysis through the operating parameter study found that the contribution of operating temperature to stress and deformation increases as the mass of the rotor is increased in seeking to meet deformation limits. Moreover, it was found to usurp gravity to become the most dominant contributor as mass is increased, as reflected by its deformation profile. Operating temperature is the only parameter to increase as both the rotor disk and cylinder thicknesses are increased, further signifying its importance.

Considering also that the same temperature presented little to no difficulty in the meeting of structural deformation limits during the parameter optimisation of the 3 MW conical rotor structure presented in [11], these findings suggest that elevated operating temperatures are of growing concern as generator sizes and masses increase, not just in terms of electrical efficiency as widely understood, but also, crucially, in the integrity of the generator itself.

Through this analysis, it was, therefore, determined that when accounting for generator operating temperature, the deformation limits of the 15 MW Reference Turbine could not be met solely by parameter optimisation, and therefore, further optimisation of the rotor through topology optimisation techniques is necessary to reduce structural mass, with the goal of consequently reducing the effects of thermal expansion. Further work investigating the effectiveness of topology optimisation in capacity will, therefore, be carried out.

Subsequent analyses of the thermal stresses during operation under dynamic conditions would be beneficial in providing a more complete view of large-scale PMDD generator operating limitations. Operating temperature is highest during extended periods of high load intensity, which further increases the risk of structural failure during these moments. Providing a clearer view of the structure's temperatures during operation would provide better understanding of the extent of temperature's influence on generator structural integrity.

Using the SolidWorks Sustainability tool, an estimate of the environmental impact of the rotor was made, finding significantly increased $CO_2$ emissions, water usage and energy requirements in production, due to the increase in mass required in order to produce a structurally compliant design.

Cost and financial impact estimates for the initial and optimised rotors were also produced, likewise finding considerable increases in costs attributable to the additional material required for meeting structural deformation limits. With the greatly increased environmental and cost impacts consequent to meeting operating deformation and stress limits, accounting for these factors early in the design cycle has the potential to create time, monetary and environmental savings from the outset. This work will be expanded with the investigation of more complex, topology-optimised geometries.

Whilst complex, lightweight designs achieved through the likes of topology optimisation may be necessary to reduce the financial and environmental impact of the part, further investigation will be required to establish whether introducing the additional manufacturing steps required for more complex designs will indeed result in cost savings. Future work will aim to determine the financial and environmental impact of operating temperature's effect on the structure. It will also aim to develop a simultaneous, integrated, iterative approach to optimisation, including Life Cycle Analysis and costing analyses that can capitalise on more ambitious optimisation strategies. This is imperative to not only determine and improve generator structural efficiencies and performance, but importantly, also environmental impacts and financial costs, and may yield compounding improvements to the aforementioned, when complimented by topology optimisation.

**Author Contributions:** Conceptualization, M.B., A.J. and P.J.-S.; methodology, P.J.-S.; formal analysis, M.B. and A.J.; investigation, M.B.; resources, P.J.-S.; data curation, M.B. and A.J.; writing—original draft preparation, M.B.; writing—review and editing, M.B. and P.J.-S.; supervision, P.J.-S.; project administration, P.J.-S.; funding acquisition, P.J.-S. All authors have read and agreed to the published version of the manuscript.

**Funding:** This research was funded by EPSRC through the Future Electrical Machines Manufacturing, "FEMM", Hub, grant number 155683.

**Data Availability Statement:** The data presented in this study are available on request from the corresponding author.

**Conflicts of Interest:** The authors declare no conflict of interest.

## Appendix A

**Table A1.** Full results of the operating parameter study.

| Geometry Parameters | | | | | Shear | | Normal | | Centrifugal | |
|---|---|---|---|---|---|---|---|---|---|---|
| **Geometries** | **Cylinder Thickness (mm)** | **Disk Thickness (mm)** | **Mass (kg)** | **Mass Increase (%)** | **Deformation (mm)** | **Stress (MPa)** | **Deformation (mm)** | **Stress (MPa)** | **Deformation (mm)** | **Stress (MPa)** |
| Unmodified | 127.32 | 81.75 | 122569.2 | 0.0% | 0.574 | 31.533 | 1.515 | 20.635 | 0.017 | 0.244 |
| Both 1 | 157.32 | 111.75 | 159293.3 | 30.0% | 0.432 | 23.050 | 1.117 | 16.649 | 0.014 | 0.226 |
| Both 2 | 187.32 | 141.75 | 196587.9 | 60.4% | 0.336 | 18.182 | 0.873 | 14.251 | 0.012 | 0.217 |
| Both 3 | 217.32 | 171.75 | 234457.0 | 91.3% | 0.279 | 15.000 | 0.712 | 12.788 | 0.011 | 0.216 |
| Both 4 | 247.32 | 201.75 | 272904.5 | 122.7% | 0.240 | 12.795 | 0.600 | 11.632 | 0.010 | 0.216 |
| Both 5 | 277.32 | 231.75 | 311934.5 | 154.5% | 0.210 | 11.123 | 0.517 | 10.683 | 0.010 | 0.216 |
| Both 6 | 307.32 | 261.75 | 351551.0 | 186.8% | 0.187 | 9.847 | 0.454 | 9.888 | 0.009 | 0.217 |
| Unmodified | 127.32 | 81.75 | 122569.2 | 0.0% | 0.574 | 31.533 | 1.515 | 20.635 | 0.017 | 0.244 |
| Cylinder 1 | 142.32 | 81.75 | 140287.4 | 14.5% | 0.574 | 31.509 | 1.128 | 16.659 | 0.014 | 0.226 |
| Cylinder 2 | 172.32 | 81.75 | 158106.3 | 29.0% | 0.576 | 31.485 | 0.886 | 14.247 | 0.013 | 0.217 |
| Cylinder 3 | 202.32 | 81.75 | 176025.9 | 43.6% | 0.578 | 31.496 | 0.725 | 12.777 | 0.011 | 0.216 |
| Cylinder 4 | 232.32 | 81.75 | 194046.2 | 58.3% | 0.580 | 31.512 | 0.613 | 11.609 | 0.011 | 0.216 |
| Cylinder 5 | 262.32 | 81.75 | 212167.2 | 73.1% | 0.582 | 31.519 | 0.532 | 10.646 | 0.010 | 0.216 |
| Cylinder 6 | 292.32 | 81.75 | 230388.9 | 88.0% | 0.585 | 31.473 | 0.469 | 9.834 | 0.010 | 0.216 |
| Unmodified | 127.32 | 81.75 | 122569.2 | 0.0% | 0.574 | 31.533 | 1.515 | 20.635 | 0.017 | 0.244 |
| Disk 1 | 127.32 | 111.75 | 141372.8 | 15.3% | 0.423 | 23.057 | 1.478 | 20.548 | 0.016 | 0.243 |
| Disk 2 | 127.32 | 141.75 | 160145.1 | 30.7% | 0.337 | 18.171 | 1.415 | 20.441 | 0.016 | 0.242 |
| Disk 3 | 127.32 | 171.75 | 178917.5 | 46.0% | 0.281 | 14.999 | 1.329 | 20.288 | 0.015 | 0.240 |
| Disk 4 | 127.32 | 201.75 | 197689.8 | 61.3% | 0.241 | 12.790 | 1.231 | 20.157 | 0.014 | 0.239 |
| Disk 5 | 127.32 | 231.75 | 216462.1 | 76.6% | 0.212 | 11.128 | 1.129 | 20.050 | 0.013 | 0.238 |
| Disk 6 | 127.32 | 261.75 | 235234.5 | 91.9% | 0.189 | 9.857 | 1.031 | 19.917 | 0.012 | 0.236 |

**Table A2.** Full results of the operating parameter study (continued).

| Gravity | | Thermal | | All Excluding Thermal | | All | |
|---|---|---|---|---|---|---|---|
| **Deformation (mm)** | **Stress (MPa)** | **Deformation (mm)** | **Stress (MPa)** | **Deformation (mm)** | **Stress (MPa)** | **Deformation (mm)** | **Stress (MPa)** |
| 23.399 | 76.884 | 2.071 | 165.370 | 24.895 | 84.698 | 24.303 | 213.900 |
| 11.065 | 48.674 | 2.087 | 167.200 | 12.174 | 55.063 | 11.737 | 190.640 |
| 6.427 | 36.550 | 2.119 | 167.800 | 7.295 | 39.828 | 7.025 | 184.690 |
| 4.221 | 28.753 | 2.148 | 168.600 | 4.930 | 32.797 | 4.841 | 178.460 |
| 3.015 | 23.462 | 2.175 | 166.750 | 3.611 | 28.046 | 3.717 | 176.530 |
| 2.282 | 20.056 | 2.200 | 172.210 | 2.796 | 24.490 | 3.116 | 174.270 |
| 1.802 | 17.827 | 2.223 | 170.640 | 2.253 | 21.653 | 2.830 | 171.600 |
| 23.399 | 76.884 | 2.071 | 165.370 | 24.895 | 84.698 | 24.303 | 213.900 |
| 26.605 | 87.630 | 2.085 | 163.170 | 27.723 | 94.315 | 27.183 | 219.520 |
| 29.965 | 102.550 | 2.116 | 161.800 | 30.843 | 103.450 | 30.349 | 229.870 |
| 33.445 | 114.360 | 2.144 | 161.990 | 34.160 | 115.180 | 33.685 | 239.110 |
| 36.947 | 125.410 | 2.167 | 161.710 | 37.545 | 126.480 | 37.111 | 247.110 |
| 40.417 | 132.350 | 2.190 | 162.260 | 40.933 | 136.990 | 40.511 | 259.370 |
| 44.000 | 146.210 | 2.211 | 160.870 | 44.458 | 148.830 | 44.039 | 262.050 |
| 23.399 | 76.884 | 2.071 | 165.370 | 24.895 | 84.698 | 24.303 | 213.900 |

**Table A2.** *Cont.*

| Gravity | | Thermal | | All Excluding Thermal | | All | |
|---|---|---|---|---|---|---|---|
| Deformation (mm) | Stress (MPa) | Deformation (mm) | Stress (MPa) | Deformation (mm) | Stress (MPa) | Deformation (mm) | Stress (MPa) |
| 9.840 | 44.266 | 2.069 | 166.790 | 11.302 | 50.380 | 10.833 | 186.770 |
| 5.223 | 27.762 | 2.065 | 168.820 | 6.624 | 35.149 | 6.332 | 180.340 |
| 3.187 | 20.360 | 2.073 | 169.570 | 4.506 | 27.331 | 4.408 | 177.100 |
| 2.121 | 15.192 | 2.080 | 170.500 | 3.344 | 22.780 | 3.445 | 173.290 |
| 1.500 | 12.100 | 2.093 | 170.380 | 2.622 | 20.877 | 2.910 | 169.990 |
| 1.105 | 10.263 | 2.108 | 170.690 | 2.130 | 20.659 | 2.588 | 170.100 |

## References


1. BEIS. Renewable Energy Planning Database (REPD): January 2023. 31 January 2023. Available online: https://www.gov.uk/government/publications/renewable-energy-planning-database-monthly-extract (accessed on 6 April 2023).
2. Kaiser, M.J.; Snyder, B.F. *Offshore Wind Energy Cost Modeling*; Springer: London, UK, 2012. [CrossRef]
3. Nejad, A.R.; Keller, J.; Guo, Y.; Sheng, S.; Polinder, H.; Watson, S.; Dong, J.; Qin, Z.; Ebrahimi, A.; Schelenz, R.; et al. Wind turbine drivetrains: State-of-the-art technologies and future development trends. *Wind Energy Sci.* **2022**, *7*, 387–411. [CrossRef]
4. Carroll, J.; McDonald, A.; McMillan, D. Reliability Comparison of Wind Turbines with DFIG and PMG Drive Trains. *IEEE Trans. Energy Convers.* **2015**, *30*, 663–670. [CrossRef]
5. Carroll, J.; McDonald, A.; McMillan, D. Failure rate, repair time and unscheduled O&M cost analysis of offshore wind turbines. *Wind Energy* **2016**, *19*, 1107–1119. [CrossRef]
6. Hayes, A.; Sethuraman, L.; Dykes, K.; Fingersh, L.J. Structural Optimization of a Direct-Drive Wind Turbine Generator Inspired by Additive Manufacturing. *Procedia Manuf.* **2018**, *26*, 740–752. [CrossRef]
7. Jaen-Sola, P.; McDonald, A.S.; Oterkus, E. Dynamic structural design of offshore direct-drive wind turbine electrical generators. *Ocean Eng.* **2017**, *161*, 1–19. [CrossRef]
8. Jaen-Sola, P.; Mc Donald, A.S.; Oterkus, E. Design of direct-drive wind turbine electrical generator structures using topology optimization techniques. *J. Phys. Conf. Ser.* **2020**, *1618*, 052009. [CrossRef]
9. Hayes, A.C.; Whiting, G.L. Reducing the Structural Mass of Large Direct Drive Wind Turbine Generators through Triply Periodic Minimal Surfaces Enabled by Hybrid Additive Manufacturing. *Clean Technol.* **2021**, *3*, 227–242. [CrossRef]
10. Tartt, K.; Amiri, A.K.; McDonald, A.; Jaen-Sola, P. Structural Optimisation of Offshore Direct-Drive Wind Turbine Generators Including Static and Dynamic Analyses. *J. Phys. Conf. Ser.* **2021**, *2018*, 012040. [CrossRef]
11. Jaen-Sola, P.; Oterkus, E.; McDonald, A.S. Parametric lightweight design of a direct-drive wind turbine electrical generator supporting structure for minimising dynamic response. *Ships Offshore Struct.* **2021**, *16*, 266–274. [CrossRef]
12. Alexandrova, Y.; Semken, R.S.; Pyrhönen, J. Permanent magnet synchronous generator design solution for large direct-drive wind turbines: Thermal behavior of the LC DD-PMSG. *Appl. Therm. Eng.* **2014**, *65*, 554–563. [CrossRef]
13. Polikarpova, M.; Ponomarev, P.; Röyttä, P.; Semken, S.; Alexandrova, Y.; Pyrhönen, J. Direct liquid cooling for an outer-rotor direct-drive permanent-magnet synchronous generator for wind farm applications. *IET Electr. Power Appl.* **2015**, *9*, 523–532. [CrossRef]
14. Zhao, X.; Fan, Y.; Li, W.; Li, D.; Cao, J.; Zhang, Y. Optimization of Ventilation Spacer for Direct-Drive Permanent Magnet Wind Generator. *Energies* **2019**, *12*, 1430. [CrossRef]
15. Shi, N.; Wei, M.; Zhang, L.; Hu, X.; Song, B. Design and research of cooling system for 2.5 MW permanent magnet wind turbine. *Renew. Energy* **2021**, *168*, 97–106. [CrossRef]
16. Zhao, Z.; Mei, T.; Li, J.; Liu, G. Ventilation structure design and heat transfer analysis of 3.3MW permanent magnet direct drive wind generators. *Energy Rep.* **2022**, *8*, 1280–1286. [CrossRef]
17. Bichan, M.; Jack, A.; Jaen-Sola, P. A Metal Selection and Structural Optimisation Methodology for Large-Scale Direct-Drive Wind Turbine Electrical Generators. In Proceedings of the 12th International Conference on Power Electronics, Machines and Drives (PEMD 2023), Brussels, Belgium, 23–24 October 2023.
18. Gaertner, E.; Rinker, J.; Sethuraman, L.; Zahle, F.; Anderson, B.; Barter, G.; Abbas, N.; Meng, F.; Bortolotti, P.; Skrzypinski, W.; et al. Definition of the IEA 15 MW Offshore Reference Wind Turbine. Golden, CO. 2020. Available online: https://www.nrel.gov/docs/fy20osti/75698.pdf (accessed on 10 January 2022).
19. Gaertner, E.; Rinker, J.; Sethuraman, L.; Zahle, F.; Anderson, B.; Barter, G.; Abbas, N.; Meng, F.; Bortolotti, P.; Skrzypinski, W.; et al. IEAWindTask37/IEA-15-240-RWT: 15MW Reference Wind Turbine Repository. Available online: https://github.com/IEAWindTask37/IEA-15-240-RWT (accessed on 10 April 2023).
20. Stander, J.N.; Venter, G.; Kamper, M.J. Review of direct-drive radial flux wind turbine generator mechanical design. *Wind Energy* **2012**, *15*, 459–472. [CrossRef]
21. ANSYS. *ANSYS®Academic Research Mechanical*; ANSYS: Canonsburg, PA, USA, 2022; (Release 2022R), [Computer Software].

22. BOVIA Dassault Systèmes. BOVIA SOLIDWORKS Sustainability Overview. 2020. Available online: https://help.solidworks.com/2020/english/SolidWorks/sldworks/c_Sustainability_Overview.htm (accessed on 24 April 2023).
23. BOVIA Dassault Systèmes. BOVIA SOLIDWORKS Costing Overview. 2020. Available online: https://help.solidworks.com/2018/english/SolidWorks/sldworks/c_costing_top.htm (accessed on 24 April 2023).
24. ORE Catapult. 7MW Levenmouth Demonstration Turbine—ORE. 2020. Available online: https://ore.catapult.org.uk/what-we-do/testing-validation/levenmouth/ (accessed on 27 September 2022).
25. SOLIDWORKS Sustainability Matrix | Solid Solutions. Available online: https://www.solidsolutions.co.uk/solidworks/simulation/matrix/sustainability.aspx (accessed on 26 June 2023).
26. Chen, W.; Zhang, Q.; Wang, C.; Li, Z.; Geng, Y.; Hong, J.; Cheng, Y. Environmental sustainability challenges of China's steel production: Impact-oriented water, carbon and fossil energy footprints assessment. *Ecol. Indic.* **2022**, *136*, 108660. [CrossRef]
27. Tong, Y.; Cai, J.; Zhang, Q.; Gao, C.; Wang, L.; Li, P.; Hu, S.; Liu, C.; He, Z.; Yang, J. Life cycle water use and wastewater discharge of steel production based on material-energy-water flows: A case study in China. *J. Clean. Prod.* **2019**, *241*, 118410. [CrossRef]
28. Harvey, L.D.D. Analysis of the Theoretical and Practical Energy Requirements to Produce Iron and Steel, with Summary Equations that Can Be Applied in Developing Future Energy Scenarios. *J. Sustain. Met.* **2020**, *6*, 307–332. [CrossRef]